

A Critical Comparison of Excitation Force Estimators for Wave-Energy Devices

Yerai Peña-Sanchez¹, Christian Windt, Josh Davidson, and John V. Ringwood², *Senior Member, IEEE*

Abstract—The implementation of energy-maximizing control systems (EMCSs) can significantly increase the efficiency and economic viability of resonant wave-energy converters (WECs). To achieve optimal control and drive the WEC into resonance with the incoming wave field, knowledge of the wave excitation force is required. In operational conditions, this quantity is immeasurable and, thus, has to be estimated. This article presents a critical comparison of the available excitation force estimators found in the literature. A reference measurement of the excitation force is determined using computational fluid dynamics (CFD) simulation, allowing an absolute comparison of the different estimation strategies. The estimators are compared based on the required input data, achieved accuracy, computational delay, and estimation time. In total, 11 estimation strategies are compared, with three, in particular, emerging with relatively superior performance.

Index Terms—Excitation force estimation, Kalman filter (KF), optimal control, unknown input estimation, wave energy, wave-energy converter (WEC).

I. INTRODUCTION

WAVE energy has a higher energy density than other renewable energy sources, such as solar or wind energy, and shows potential to significantly contribute to the global energy mix. However, since wave energy is still at an early stage of development, its levelized cost of energy (LCOE) is too high to be commercially competitive [1]–[3]. Therefore, considerable research effort has focused on the development of control systems to maximize energy capture. Energy-maximizing control systems (EMCSs) optimize the power output of a wave-energy converter (WEC) by driving it into resonance with the incident wave field [4].

Numerous EMCSs for WECs have been proposed in the literature [5]. For the determination of the optimal control inputs, the majority of these EMCSs require knowledge of

the instantaneous and future wave-excitation force ($F_{\text{ex}}(t)$) acting on the WEC [4]. $F_{\text{ex}}(t)$ represents the force acting on a fixed or floating body due to the incoming waves. For a fixed body, $F_{\text{ex}}(t)$ can simply be measured by integrating the pressure over the submerged body surface. However, for a nonfixed body, $F_{\text{ex}}(t)$ is an immeasurable quantity, since the integrated pressure over the submerged body surface represents the $F_{\text{ex}}(t)$ and other hydrodynamic forces, e.g., wave-radiation force ($F_{\text{R}}(t)$), wave hydrostatic restoring force ($F_{\text{H}}(t)$), and so on. Therefore, for a floating body, such as a WEC, $F_{\text{ex}}(t)$ can only be estimated. To this end, various strategies have been proposed in the literature, which attempt to estimate $F_{\text{ex}}(t)$ based on measurable quantities, such as device position and velocity or the pressure on the WEC hull.

Given the large number of published estimation strategies, knowledge of their relative strengths and weaknesses is important. Therefore, this study aims to review the $F_{\text{ex}}(t)$ estimators found in the literature, and conduct a critical and fair comparison. In this study, a total of 11 different $F_{\text{ex}}(t)$ estimators are included. To the best of our knowledge, such a comprehensive comparison has not yet been performed. Reviews of different $F_{\text{ex}}(t)$ estimators have been presented in [6]–[8]; however, these reviews only consider a maximum of three different estimation strategies.

As shown in Section III, comparing different estimators is not a trivial task. Since the $F_{\text{ex}}(t)$ on a moving body is an immeasurable quantity, the definition of an unbiased reference for the comparison poses a challenge. Therefore, this study employs computational fluid dynamics (CFD) simulation to create a benchmark for the estimator comparison. A 5-m diameter, heaving sphere, point absorber WEC is chosen as the case study for the presented comparison. The device is exposed to a realistic, polychromatic sea state and a hydraulic power take-off (PTO), with a simple resistive controller, implemented in the model.

The remainder of this article is organized as follows. Based on a complete literature review, Section II introduces the different available $F_{\text{ex}}(t)$ estimators. Next, Section III describes the methodology for the critical comparison. More information on the case study for the comparison is then presented in Section IV. Results of the comparison are shown and discussed in Section V. Finally, some conclusions are drawn in Section VI.

II. EXCITATION FORCE ESTIMATORS

Before reviewing the different estimation strategies and introducing their theoretical background, let us first define the (linear) hydrodynamic model used in the estimators to

Manuscript received January 10, 2019; revised June 6, 2019; accepted August 22, 2019. Date of publication September 18, 2019; date of current version October 9, 2020. This work was supported in part by the Science Foundation Ireland under Grant 13/IA/1886, in part by the Higher Education Excellence Program of the Ministry of Human Capacities in the frame of the Water Sciences & Disaster Prevention Research Area of BME (BME FIKP-VÍZ), and in part by the National Research, Development and Innovation Fund through the Thematic Excellence Program under Grant TUDFO/51757/2019-ITM. Recommended by Associate Editor C. Manzie. (Corresponding author: Yerai Peña-Sanchez.)

Y. Peña-Sanchez, C. Windt, and J. V. Ringwood are with the Department of Electronic Engineering, Centre for Ocean Energy Research, Maynooth University, Maynooth, W23 F2H6 Ireland (e-mail: yerai.pena.2017@mumail.ie; christian.windt.2017@mumail.ie; john.ringwood@mu.ie).

J. Davidson is with the Department of Fluid Mechanics, Faculty of Mechanical Engineering, Budapest University of Technology and Economics, 1111 Budapest, Hungary (e-mail: davidson@ara.bme.hu).

Color versions of one or more of the figures in this article are available online at <http://ieeexplore.ieee.org>.

Digital Object Identifier 10.1109/TCST.2019.2939092

1063-6536 © 2019 IEEE. Personal use is permitted, but republication/redistribution requires IEEE permission. See <https://www.ieee.org/publications/rights/index.html> for more information.

characterize the motion of a floating body, which is a form of Cummin's equation [9], and is defined as

$$m^* \ddot{z}(t) + F_R(t) + F_H(t) + F_{PTO}(t) = F_{ex}(t) \quad (1)$$

where $m^* = m + A_\infty$, m is the mass of the body, and A_∞ the infinite-frequency added mass. z , \dot{z} , and \ddot{z} denote the heave¹ position, velocity, and acceleration of the device (see Fig. 1), respectively. t denotes time, $F_R(t) = \int_{t_0}^t k_R(t - \tau) \dot{z}(\tau) d\tau$, k_R is the radiation force impulse response, $F_H(t) = S_H z(t)$, S_H is the hydrostatic stiffness due to buoyancy, $F_{PTO}(t) = D_{PTO} \dot{z}(t)$ is the force of the PTO system, and D_{PTO} is the PTO-damping term. Assuming that the convolution term of the radiation force is approximated using a parametric model, as shown in [10], (1) can be expressed by the following continuous-time state-space model:

$$\dot{x}(t) = Ax(t) + BF_{ex}(t) \quad (2a)$$

$$y(t) = Cx(t) + DF_{ex}(t) \quad (2b)$$

where $x(t) = [z(t) \dot{z}(t) x_R(t)]^T$, $x_R(t) \in \mathbb{R}^{n_R}$ is the state vector of the radiation force convolution term approximation, $y(t) = [z(t) \dot{z}(t) \ddot{z}(t)]^T$, and the matrices $A \in \mathbb{R}^{n \times n}$, $B \in \mathbb{R}^n$, $C \in \mathbb{R}^{q \times n}$, and $D \in \mathbb{R}^q$ are given by

$$\begin{aligned} A &= \begin{bmatrix} 0 & 1 & 0 \\ -S_H & -D_{PTO} & -C_R \\ \frac{m^*}{0} & \frac{m^*}{B_R} & \frac{m^*}{A_R} \end{bmatrix} \\ B &= \begin{bmatrix} 0 \\ 1 \\ \frac{m^*}{0} \end{bmatrix} \\ C &= \begin{bmatrix} 1 & 0 & 0 \\ 0 & 1 & 0 \\ -S_H & -D_{PTO} & -C_R \\ \frac{m^*}{m^*} & \frac{m^*}{m^*} & \frac{m^*}{m^*} \end{bmatrix} \\ D &= \begin{bmatrix} 0 \\ 0 \\ 1 \\ \frac{m^*}{m^*} \end{bmatrix}. \end{aligned} \quad (3)$$

Here, $n = 2 + n_R$ refers to the number of states, the symbol 0 stands for any zero element dimensioned according to the context, and $A_R \in \mathbb{R}^{n_R \times n_R}$, $B_R \in \mathbb{R}^{n_R}$, and $C_R \in \mathbb{R}^{n_R}$ are the matrices of the state-space model for the approximation of the radiation force convolution term. Although the default outputs of system (2) are position, velocity, and acceleration of the device, matrices C and D will be changed according to the requirements of the different estimators. In addition, the discrete-time equivalent of system (2) is given by

$$x(k+1) = A^d x(k) + B^d F_{ex}(k) \quad (4a)$$

$$y(k) = Cx(k) + DF_{ex}(k) \quad (4b)$$

where k is the discrete time index ($t = kT_s$), with sampling time T_s , and A^d and B^d refer to the discretized versions of the matrices A and B , respectively, which can be computed from system (2), as shown in [11].

Having defined the hydrodynamic model, the review of the available estimators is presented in Sections II-A–II-J.

¹For the sake of simplicity, only the heave motion is considered in this work.

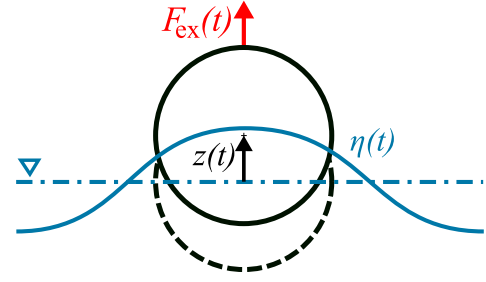


Fig. 1. Schematic of the heaving sphere point absorber WEC.

Information on the theory of the different estimation strategies is kept to a minimum, for brevity. The interested reader is referred to the provided references, for a more comprehensive description of the different approaches. Based on the review of the available estimators, some possible classifications of the strategies are proposed in Section II-K.

A. Convolution With Predicted Wave Elevation

The convolution with predicted wave elevation (CPWE) $F_{ex}(t)$ estimation strategy is based on the convolution product between the wave elevation ($\eta(t)$) and the excitation force impulse-response function ($IRF_{F_{ex}}(t)$). The $IRF_{F_{ex}}(t)$ can be obtained via inverse Fourier transform of the frequency-response function (FRF) of the $F_{ex}(t)$, which, in turn, can be computed using the boundary-element method (BEM) codes, such as NEMOH [12] or WAMIT [13]. Another way to obtain the $IRF_{F_{ex}}(t)$ is to identify it directly from physical wave tank tests, as shown in [14].

The identification of the $IRF_{F_{ex}}(t)$ for the CPWE estimator has three main drawbacks as follows.

- 1) Obtaining reliable $\eta(t)$ measurements in a real multi-directional sea scenario is a nontrivial task [15].
- 2) The $IRF_{F_{ex}}(t)$ is noncausal [16]. Hence, future $\eta(t)$ values (at the device location) are required in order to obtain the instantaneous $F_{ex}(t)$ acting on the device and must therefore be predicted. For the prediction, the required time horizon (T_{hor}) depends on the causalization time (t_{caus}) of the $IRF_{F_{ex}}(t)$, which, in turn, depends on the geometry (or the scale) of the device under analysis.
- 3) For nonaxisymmetric bodies, the $IRF_{F_{ex}}(t)$ will be different, depending on the wave direction. Therefore, in a real sea-state scenario, the different directional components of $\eta(t)$ need to be known (or estimated) in order to estimate the $F_{ex}(t)$ acting on the WEC.

Having identified the $IRF_{F_{ex}}(t)$, the estimated $F_{ex}(t)$ for the CPWE strategy (\tilde{F}_{ex}^{CPWE}) is given by

$$\tilde{F}_{ex}^{CPWE}(t) = \int_{-\infty}^{t+t_{caus}} k_{F_{ex}}^{caus}(t+t_{caus}-\tau) \hat{\eta}(\tau) d\tau \quad (5)$$

where $k_{F_{ex}}^{caus}$ is the causalized $IRF_{F_{ex}}(t)$, and $\hat{\eta}(\tau)$ refers to past values of $\eta(t)$ for $\tau < t$, the instantaneous $\eta(t)$ for $\tau = t$, and predicted values of $\eta(t)$ for $\tau > t$. This is further explained in Section V-A.

Despite the aforementioned drawbacks, the CPWE strategy is used in [8] and [17]. Owing to the small device scale, the required causalization time is around 1 s, for which an autoregressive (AR) model gives reasonably accurate

predictions of $\eta(t)$, using only past values, measured near the WEC.² In addition, the $k_{F_{\text{ex}}}^{\text{caus}}$ is approximated using a finite-order parametric model in order to reduce the computational burden for evaluating the convolution product [8].

As demonstrated in [18], the accuracy of the η prediction obtained using only past data decreases exponentially with an increase in T_{hor} . Therefore, for longer causalization times, measurements from several points near the device may be needed to increase the prediction accuracy [19]. Such a technique is employed in [20], where $\eta(t)$ is predicted using up-wave information provided by a Doppler radar, positioned at the WEC location. The required number of up-wave measurement points to obtain an accurate prediction will depend, mostly, on the directionality of the sea state, i.e., using the information from a unique point can be enough for unidirectional sea states [19]. In general, it can be stated that the accuracy of the $F_{\text{ex}}(t)$ estimate, using the CPWE strategy, will depend on both the accuracy of the $\eta(t)$ prediction and the definition of the IRF $_{F_{\text{ex}}}(t)$.

B. Kalman Filter With Random Walk

Omitting the use of $\eta(t)$ for $F_{\text{ex}}(t)$ estimation, the Kalman filter with random walk (KFRW) strategy considers $F_{\text{ex}}(t)$ as an unknown input to the system and estimates the force, based on the device motion measurements, using an observer. The motion of the device (along with the corresponding $F_{\text{ex}}(t)$) is estimated and compared with the measured motion. Therefore, the accuracy of the obtained $F_{\text{ex}}(t)$ estimation will highly depend on how accurate the model, used in the KF, represents the actual WEC. The dynamical model of the excitation force is given by

$$F_{\text{ex}}^{\text{KFRW}}(k+1) = F_{\text{ex}}^{\text{KFRW}}(k) + \epsilon_{F_{\text{ex}}}(k) \quad (6)$$

where $\epsilon_{F_{\text{ex}}}(k)$ is a random number (independently and identically distributed in size), so that, at each time step, $F_{\text{ex}}^{\text{KFRW}}$ takes a random step away from its previous value. The augmented model, including the dynamical description of $F_{\text{ex}}(t)$, is defined as

$$\tilde{x}_a(k+1) = A_a^d \tilde{x}_a(k) + \epsilon(k) \quad (7a)$$

$$\tilde{y}(k) = C_a \tilde{x}_a(k) + \mu(k). \quad (7b)$$

Here, the subscript $\{\cdot\}_a$ refers to the augmented $\{\cdot\}$, and $A_a^d \in \mathbb{R}^{(n+1) \times (n+1)}$, $C_a \in \mathbb{R}^{q \times (n+1)}$, and $\tilde{x}_a \in \mathbb{R}^{(n+1)}$ are given by

$$\tilde{x}_a = \begin{bmatrix} \tilde{x} \\ \tilde{F}_{\text{ex}}^{\text{KFRW}} \end{bmatrix}, \quad A_a^d = \begin{bmatrix} A^d & B^d \\ 0 & 1 \end{bmatrix}, \quad C_a = [C \quad 0] \quad (8)$$

where $\epsilon(k)$ and $\mu(k)$ are the process and measurement white-noises, whose covariance matrices are Q and R , respectively. In addition, C is modified in this strategy to obtain just the position and velocity as outputs.

It is now possible to define the linear, discrete-time KF used by KFRW as follows:

Time Update (A Priori) :

$$\tilde{x}_a^-(k) = A_a^d \tilde{x}_a^-(k-1) \quad (9a)$$

$$P^-(k) = A_a^d P^-(k-1) A_a^{dT} + Q. \quad (9b)$$

²It can be assumed to be equal to η in the WEC location, since waves come from a unique direction.

Measurement Update (A Posteriori) :

$$K(k) = P^-(k) C_a^T (C_a P^-(k) C_a^T + R)^{-1} \quad (9c)$$

$$P(k) = (\mathbf{I}_{n+1} - K(k) C_a) P^-(k) \quad (9d)$$

$$\tilde{x}_a(k) = \tilde{x}_a^-(k) + K(k) (y(k) - C_a \tilde{x}_a^-(k)) \quad (9e)$$

where the superscript $\{\cdot\}^-$ denotes the *a priori* estimate of $\{\cdot\}$ and $\{\cdot\}^T$ the transpose of $\{\cdot\}$. \mathbf{I}_{n+1} stands for the identity matrix of size $(n+1) \times (n+1)$. The reader is referred to [21] for more information on the KF. As demonstrated in [7], the KFRW strategy is simple and, by using a KF, can optimally handle the measurement noise (if the measurement noise is Gaussian).

C. Kalman Filter With Harmonic Oscillator

While the KFRW estimator uses a random walk (RW) model to describe the $F_{\text{ex}}(t)$ dynamics, the Kalman filter with a harmonic oscillator (KFHO) uses a KF in conjunction with a harmonic oscillator (HO) model to describe the dynamics of the $F_{\text{ex}}(t)$. Therefore, the same process introduced for the KFRW can be used for the KFHO, with an adaptation of the matrices shown in (8), which are now given by

$$A_a^d = \begin{bmatrix} A^d & B^d C_{\text{HO}} \\ 0 & \Omega_{\text{HO}} \end{bmatrix}, \quad \tilde{x}_a = \begin{bmatrix} \tilde{x} \\ \tilde{\Theta} \end{bmatrix} \quad (10)$$

where $\Omega_{\text{HO}} \in \mathbb{R}^{2n_\omega \times 2n_\omega}$ and $\tilde{\Theta} \in \mathbb{R}^{2n_\omega}$ are defined as

$$\Omega_{\text{HO}} = \bigoplus_{i=1}^{n_\omega} \begin{bmatrix} 0 & \omega_i \\ -\omega_i & 0 \end{bmatrix}, \quad \tilde{\Theta} = \sum_{i=1}^{n_\omega} e_i^{n_\omega} \otimes \begin{bmatrix} \tilde{\theta}_{\omega_i} \\ \dot{\tilde{\theta}}_{\omega_i} \end{bmatrix} \quad (11)$$

where ω_i , with $i = (1, 2, \dots, n_\omega)$, are the frequencies of the HO describing $F_{\text{ex}}(t)$, and the symbols $\bigoplus_{i=1}^{n_\omega}$ and \otimes stand for the direct sum of n_ω matrices and the Kronecker product, respectively. $e_i^{n_\omega} \in \mathbb{R}^{n_\omega \times 1}$ denotes a vector with 1 in the i th entry, and 0 elsewhere, and $C_{\text{HO}} = \sum_{i=1}^{n_\omega} e_i^{n_\omega T} \otimes [1 \ 0]$. The estimated $F_{\text{ex}}(t)$ is given by

$$\tilde{F}_{\text{ex}}^{\text{KFHO}}(k) = \sum_{i=1}^{n_\omega} \tilde{\theta}_{\omega_i}(k). \quad (12)$$

Overall, this strategy is the most commonly used $F_{\text{ex}}(t)$ estimator in the literature. In [6] and [22]–[24], the KFHO approach is used to estimate the excitation force acting on a heaving point absorber. In [25], the model used for the KFHO strategy is amplified to include all the interactions between the devices for different array configurations. In addition, Ling [24] presents an approach for the calculation of the best parameters for the KFHO estimator, based on optimization.

D. Extended Kalman Filter Harmonic Oscillator

In the extended KFHO (EKFHO), the HO model is described by time-varying frequencies, allowing for the estimation of the dominant frequencies of the $F_{\text{ex}}(t)$. For the treatment of time-varying frequencies, the extended KF (EKF) is employed [6], [24].

In addition to estimating the instantaneous $F_{\text{ex}}(t)$ frequency, Fusco and Ringwood [26] adapt the EKFHO to also estimate its instantaneous amplitude. A further extension is presented in [27], where the amplitude, frequency, and phase of the

different components of the $F_{\text{ex}}(t)$ signal are estimated. Among the previously described variations in the EKFHO strategy, the most complete one is chosen for this work, estimating the $F_{\text{ex}}(t)$ amplitude, frequency, and phase [27]. Therefore, the $F_{\text{ex}}^{\text{EKFHO}}(t)$ is defined using multiple harmonic signals

$$F_{\text{ex}}^{\text{EKFHO}}(t) = \sum_{i=1}^{n_\omega} \lambda_i \sin(\omega_i t + \phi_i) \quad (13)$$

where λ_i and ϕ_i are the corresponding amplitudes and phases.

The only difference between the continuous–discrete EKF, used by the EKFHO strategy, and the KF shown in (9) is the Time Update part [see (9a) and (9b)]. In the EKFHO, $\tilde{x}_a^-(k)$ is obtained by propagating the state at the previous measurement time, $(k-1)$, as

$$\dot{\tilde{x}}_a(t) = A_a \tilde{x}_a(t) + B_a \tilde{F}_{\text{ex}}^{\text{EKFHO}}(t) + \epsilon(t) \quad (14)$$

where $A_a \in \mathbb{R}^{(n+3n_\omega) \times (n+3n_\omega)}$ and $\tilde{x}_a \in \mathbb{R}^{(n+3n_\omega)}$ are defined as

$$A_a = \begin{bmatrix} A & 0 \\ 0 & 0 \end{bmatrix} \quad \tilde{x}_a = [\tilde{x}^T \quad \tilde{\Lambda}^T \quad \tilde{\Omega}^T \quad \tilde{\Phi}^T]^T. \quad (15)$$

$\tilde{\Lambda}$, $\tilde{\Omega}$, and $\tilde{\Phi} \in \mathbb{R}^{n_\omega}$ are the vectors containing the estimates of λ , ω , and ϕ , respectively. It should be noted that the continuous–discrete EKF, used by this estimation strategy, combines continuous-time nonlinear models with discrete-time measurements and, therefore, the notation corresponding to both continuous- and discrete-time are mixed in the definition of the strategy, as shown in [21] and [28].

The covariance matrix $P^-(k)$, of (9b), is propagated from the previous measurement time, $(P(k-1))$, using the following Riccati equation:

$$\dot{P}(t) = \Upsilon(\tilde{x}_a(t))P(t) + P(t)\Upsilon^T(\tilde{x}_a(t)) + Q \quad (16)$$

where

$$\Upsilon(\tilde{x}_a(t)) = \begin{bmatrix} A & B\Psi(\tilde{x}_a(t)) \\ 0 & 0 \end{bmatrix} \quad (17)$$

is computed using $\tilde{x}_a(k-1)$, and

$$\Psi = \begin{bmatrix} \frac{\partial \tilde{F}_{\text{ex}}^{\text{EKFHO}}}{\partial \tilde{\Lambda}} & \frac{\partial \tilde{F}_{\text{ex}}^{\text{EKFHO}}}{\partial \tilde{\Omega}} & \frac{\partial \tilde{F}_{\text{ex}}^{\text{EKFHO}}}{\partial \tilde{\Phi}} \end{bmatrix}. \quad (18)$$

E. Receding Horizon Estimation

Also considering $F_{\text{ex}}(t)$ as an unknown input, the receding horizon estimation (RHE) strategy estimates $F_{\text{ex}}(t)$ without assuming any dynamical model, employing RHE [7]. Nguyen and Tona [7] claim that avoiding a dynamical model for $F_{\text{ex}}(t)$ improves the obtained results. At every time instant $k > N$ (where N is the length of the moving window), $F_{\text{ex}}(t)$ is estimated by minimizing the quadratic programming problem shown in [7]. However, since no constraint is considered in this work, the unique analytical solution of such a quadratic programming problem can be obtained as

$$\tilde{\xi}^*(k) = (\mathbf{P} + \Psi_s^T \mathbf{R} \Psi_s)^{-1} [\mathbf{S}^T \quad \Psi_s^T \mathbf{R}^T] \begin{bmatrix} \tilde{F}_{\text{ex}}^{\text{RHE}}(k-N) \\ \tilde{x}(k-N) \\ Y(k) \end{bmatrix} \quad (19)$$

where $\mathbf{R} \in \mathbb{R}^{qN \times qN}$ is a diagonal weighting matrix to account for the measurement noise, $Y(k) \in \mathbb{R}^{qN}$ is a vector containing all the values of y (assuming z and \dot{z} as outputs) from $k-N+1$ to k , $\Psi_s = [\Psi_y \quad \Phi_y \quad \Gamma_y] \in \mathbb{R}^{qN \times (N+n+nN)}$, and the matrices $\mathbf{P} \in \mathbb{R}^{(N+n+nN) \times (N+n+nN)}$, $\Psi_y \in \mathbb{R}^{qN \times N}$, $\Phi_y \in \mathbb{R}^{qN \times n}$, $\Gamma_y \in \mathbb{R}^{qN \times nN}$, and $\mathbf{S} \in \mathbb{R}^{(1+n) \times (N+n+nN)}$ are given by system (20).

In system (20), $P_0^{-1} \in \mathbb{R}^{n \times n}$ is a diagonal weighting matrix, penalizing the error in the state estimate, $\mathbf{Q} \in \mathbb{R}^{nN \times nN}$ is a diagonal weighting matrix, penalizing the process noise, and $Q_0^{-1} \in \mathbb{R}$ a scalar, penalizing the error of the $F_{\text{ex}}(t)$ estimation. The size of the second column of \mathbf{S} (which is full of zeros) is $(n+1) \times (n+1)$, and $\lambda^s \in \mathbb{R}$ is a scalar to exploit the fact that $F_{\text{ex}}(t)$ is smooth, which was first considered in [7]. To this end, the value of $\tilde{F}_{\text{ex}}^{\text{RHE}}(k)$ is given by the N th value of the vector $\tilde{\xi}^*(k) \in \mathbb{R}^{(N+n+nN)}$ of (19)

$$\begin{aligned} \mathbf{P} &= \begin{bmatrix} \Lambda_1 & 0 & 0 \\ 0 & P_0^{-1} & 0 \\ 0 & 0 & \mathbf{Q} \end{bmatrix} \\ \Gamma_y &= \begin{bmatrix} C & 0 & \dots & 0 \\ CA & C & \dots & 0 \\ \vdots & \vdots & \ddots & \vdots \\ CA^{N-1} & CA^{N-2} & \dots & C \end{bmatrix} \\ \Psi_y &= \begin{bmatrix} CB & 0 & \dots & 0 \\ CAB & CB & \dots & 0 \\ \vdots & \vdots & \ddots & \vdots \\ CA^{N-1}B & CA^{N-2}B & \dots & CB \end{bmatrix} \\ \Phi_y &= \begin{bmatrix} CA \\ CA^2 \\ \vdots \\ CA^N \end{bmatrix} \\ \Lambda_1 &= \begin{bmatrix} Q_0^{-1} + \lambda^s & -\lambda^s & 0 & \dots & 0 \\ -\lambda^s & 2\lambda^s & -\lambda^s & \dots & 0 \\ 0 & -\lambda^s & 2\lambda^s & \dots & 0 \\ \vdots & \vdots & \vdots & \ddots & \vdots \\ 0 & 0 & 0 & \dots & \lambda^s \end{bmatrix} \\ \mathbf{S} &= \begin{bmatrix} Q_0^{-1} & 0 & 0 & 0 \\ 0 & 0 & P_0^{-1} & 0 \end{bmatrix}. \end{aligned} \quad (20)$$

F. Fast Adaptive Unknown Input Estimation

The fast adaptive unknown input estimation (FAUIE) observer, proposed in [15], attempts to ensure fast and accurate estimation of $F_{\text{ex}}(t)$ by using proportional and integral terms of the state estimation error as³

$$\dot{\tilde{x}}(t) = A\tilde{x}(t) + B\tilde{F}_{\text{ex}}^{\text{FAUIE}}(t) - L_1 e_y(t) - L_2 \dot{e}_y(t) \quad (21a)$$

$$\tilde{y}(t) = C\tilde{x}(t) \quad (21b)$$

where $\tilde{F}_{\text{ex}}^{\text{FAUIE}}(t) = -\Gamma L_3 C(\dot{e}_x(t) + \sigma e_x(t))$, $e_y(t) = \tilde{y}(t) - y(t)$, and $e_x(t) = \tilde{x}(t) - x(t)$. $\Gamma \in \mathbb{R}$ is the user-defined learning rate, $L_2 \in \mathbb{R}^{n \times q}$ and $\sigma \in \mathbb{R}$ are the design

³Since the used model is linear, the Lipschitz term in [15], accounting for the nonlinearities, has been removed for this work.

parameters, and both $L_1 \in \mathbb{R}^{n \times q}$ and $L_3 \in \mathbb{R}^q$ are obtained by solving the following set of linear matrix inequalities (LMIs):

$$\begin{bmatrix} \Pi_{11} & \Pi_{12} & P_L & 0 \\ \star & \Pi_{22} & 0 & B P_L \\ \star & \star & -\alpha \mathbf{I}_n & 0 \\ \star & \star & \star & \Pi_{44} \end{bmatrix} < 0 \quad (22a)$$

$$\begin{bmatrix} \bar{v} \mathbf{I}_n & B P_L - L_3 C \\ \star & \bar{v} \mathbf{I}_n \end{bmatrix} > 0. \quad (22b)$$

Here, $\Pi_{11} = he(P_L A - Y_L C)$, $Y_L = P_L L_1$, $\Pi_{12} = (\bar{\gamma}/\sigma)(C^T Y_L^T B - A^T P_L B)$, $\Pi_{22} = -(2\bar{\gamma}/\sigma)B^T P_L B + (G_L/\sigma \bar{\mu})$, $\Pi_{44} = -(\beta\sigma/\bar{\gamma})\mathbf{I}_n$, $he(\cdot) = \{\cdot\} + \{\cdot\}^T$, \star denotes the symmetric part of the matrix, and $\alpha, \beta, \bar{\mu}$, and $\bar{\gamma} > 0 \in \mathbb{R}$ are the design parameters. Although the matrix C in (21) is modified to obtain $\tilde{y} = [\tilde{z} \ \tilde{\zeta}]$, measurements of the WEC acceleration are also needed due to the term \dot{e}_y . To this end, the observer of (21) will give bounded estimation errors, $e_x(t)$ and $e_{F_{ex}}(t)$, if positive-definite matrices $P_L \in \mathbb{R}^{n \times n}$ and $G_L \in \mathbb{R}$ exist, and the constraints imposed in (22) hold, while, at the same time, $\bar{v} > 0 \in \mathbb{R}$ is minimized.

The main drawback of the FAUIE estimator is that there is no term to account for the measurement noise, which may significantly affect the accuracy of the estimated $F_{ex}(t)$.

G. Unknown Input Observer

The authors of the FAUIE, Abdelrahman *et al.* [15], present another estimation strategy, termed unknown input observer (UIO) [29]. The UIO of the application example, found in [8], is designed to robustly estimate both $F_{ex}(t)$ and velocity of the WEC. However, the UIO proposed for this work uses position and velocity measurements (instead of position and PTO current as in [8]). Before defining the required observer, the following augmented system needs to be formulated:

$$\dot{x}_a(t) = A_a x_a(t) + D_a d(t, x) \quad (23a)$$

$$y(t) = C_a x_a(t) \quad (23b)$$

where $x_a \in \mathbb{R}^{n+2}$, $A_a \in \mathbb{R}^{(n+2) \times (n+2)}$, $D_a \in \mathbb{R}^{(n+2) \times 3}$, and $C_a \in \mathbb{R}^{q \times (n+2)}$ are defined as

$$x_a(t) = \begin{bmatrix} x(t) \\ F_{ex}(t) \\ \tilde{\zeta}(t) \end{bmatrix}, A_a = \begin{bmatrix} A & B & 0 \\ 0 & 0 & 0 \\ 0 & 0 & 0 \end{bmatrix}, D_a = \begin{bmatrix} D & 0 & 0 \\ 0 & 1 & 0 \\ 0 & 0 & 1 \end{bmatrix} \\ C_a = [C \quad 0 \quad \tilde{\Xi}], \text{ with } D = [0 \quad 1]^T \text{ and } \tilde{\Xi} = [-2 \quad 2]^T. \quad (24)$$

The term $d(t, x)$ can represent a model disturbance, while $\tilde{\zeta}(t) \in \mathbb{R}^s$ stands for any measurement noise or sensor fault, with $s = 1$ for this work, representing only measurement noise. The following observer is then used to estimate the augmented state x_a :

$$\dot{\zeta}(t) = \mathcal{M}\zeta + Ly(t) \quad (25a)$$

$$\tilde{x}_a(t) = \zeta(t) + Hy(t) \quad (25b)$$

where matrices $\mathcal{M} \in \mathbb{R}^{(n+1+s) \times (n+1+s)}$, $L \in \mathbb{R}^{(n+1+s) \times q}$, and $H \in \mathbb{R}^{(n+1+s) \times q}$ are obtained, as in the FAUIE estimator, by solving the set of LMIs shown in (26). Thus, the estimation error dynamics are stable and H_∞ performance is guaranteed

with an attenuation level of γ , if there exists a symmetric positive-definite matrix $P_L \in \mathbb{R}^{(n+1+s) \times (n+1+s)}$, and the following LMI constraint holds:

$$\begin{bmatrix} he(P_L A_a - M_1 C_a A_a - M_2 C_a) & P_L D_a & C_a^T \\ \star & -\gamma \mathbf{I}_{(q+1+s)} & 0 \\ \star & \star & -\gamma \mathbf{I}_q \end{bmatrix} < 0 \quad (26)$$

where $M_1 = P_L H$, $M_2 = P_L L_1$, $L = L_1 + L_2$, $L_2 = (E A_a - L_1 C_a)H$, $E = \mathbf{I}_{(n+1+s)} - H C_a$, and $\mathcal{M} = E A_a - L_1 C_a$.

The two main advantages of the UIO strategy are that the LMIs can be designed such that the observer is robust against model uncertainties and that measurement noise can be accounted for.

H. Unified Linear Input and State Estimator

Coe and Bacelli [30] introduce the unified linear input and state estimator (ULISE), which can be shown as a generalization of the KF for systems with unknown inputs [31]. Although two variants of the ULISE strategy are presented in [30], one using only WEC motion information and another one using pressure measurements, only the one using motion measurements is employed in this comparison. The estimator using pressure measurements requires a model that relates total pressure and $F_{ex}(t)$, which is identified through wave tank tests [32] in [30]. However, this model identification was not possible for this study.

The three-phase filter proposed for the ULISE approach is defined as follows.

Time Update:

$$\tilde{x}^-(k) = A^d \tilde{x}^-(k-1) + B^d \tilde{F}_{ex}^{ULISE}(k-1) \quad (27a)$$

$$P_x^-(k) = A^d P_x^-(k-1) A^{dT} + B^d P_{x F_{ex}}^T(k-1) A^{dT} + Q \\ + A^d P_{x F_{ex}}(k-1) B^{dT} \\ + B^d P_{F_{ex}}(k-1) B^{dT} \quad (27b)$$

$$\bar{R}(k) = C P_x^-(k) C^T. \quad (27c)$$

Measurement Update:

$$K(k) = P_x^-(k) C^T \bar{R}^{-1}(k) \quad (27d)$$

$$L(k) = K(k) (\mathbf{I}_n - D(D^T \bar{R}^{-1}(k) D)^{-1} D^T \bar{R}^{-1}(k)) \quad (27e)$$

$$\tilde{x}(k) = \tilde{x}^-(k) + L(k)(y(k) - C \tilde{x}^-(k)) \quad (27f)$$

$$P_x(k) = (\mathbf{I}_n - L(k)C) P_x^-(k) (\mathbf{I}_n - L(k)C)^T \\ + L(k) R L^T(k). \quad (27g)$$

Estimation of Unknown Input:

$$\bar{R}^*(k) = (\mathbf{I}_n - CL(k)) \bar{R}(k) (\mathbf{I}_n - CL(k))^T \quad (27h)$$

$$P_{F_{ex}}(k) = (D^T \bar{R}^{*-1}(k) D)^{-1} \quad (27i)$$

$$M(k) = P_{F_{ex}}(k) D^T \bar{R}^{*-1}(k) \quad (27j)$$

$$\tilde{F}_{ex}^{ULISE}(k) = M(k)(y(k) - C \tilde{x}(k)) \quad (27k)$$

$$P_{x F_{ex}}(k) = -P_x(k) C^T M^T(k) + L(k) R M^T(k) \quad (27l)$$

where $P_x \in \mathbb{R}^{n \times n}$, $P_{F_{ex}} \in \mathbb{R}$, and $P_{x F_{ex}} \in \mathbb{R}^n$ are the covariance matrices related to the state, $F_{ex}(t)$, and the relation between the state and $F_{ex}(t)$, respectively. Since only position and acceleration measurements are used here, only the first and third rows of C and D from system (4) are considered.

I. Pressure Acceleration Displacement Estimation

The pressure acceleration displacement estimation (PADE) strategy proposed in [8] depends on the availability of pressure measurement over the wetted surface of the device. $F_{\text{ex}}(t)$ is estimated by subtracting all hydrodynamic forces (estimated using motion measurements) other than $F_{\text{ex}}(t)$ from the total wave force ($F_w(t)$), which can be calculated by integrating the pressure over the wetted surface of the WEC [8]. $F_{\text{ex}}(t)$ can thus be approximated as

$$\tilde{F}_{\text{ex}}^{\text{PADE}}(t) = A_{\infty}\ddot{z}(t) + F_R(t) + F_H - F_w(t) + gm \quad (28a)$$

$$F_w(t) = \sum_{j=1}^{n_p} P_j(t) a_j \vec{n}_j \quad (28b)$$

where g is the gravitational constant, n_p is the number of pressure sensors, $P_j(t)$ is the total pressure measured by the j th sensor, a_j is the surface area around the sensor j , and \vec{n}_j is the normal vector to a_j . Although the term gm is not included in [8], it was found that this term is required to cancel out an offset of the total pressure P .

The main disadvantage of PADE is that, since it cannot handle measurement noise, signals need to be filtered before using them for the estimation.

J. Extended Kalman Filter With Pressure Sensors

The last estimation technique found in the reviewed literature and considered in this study uses an extended Kalman filter with pressure sensors (EKFPS) [28], [33]. Here, $F_{\text{ex}}(t)$ estimation is carried out recursively by an EKF, using the measurements of device position and pressure on the WEC hull. $F_{\text{ex}}(t)$ is then modeled as the integration of the excitation pressure [see (30)] over the wetted WEC surface, which assumes that $F_{\text{ex}}(t)$ is given only by the Froude Krylov force, neglecting the diffraction forces. Since the experiments are carried out in deep-water waves, the $\tilde{F}_{\text{ex}}^{\text{EKFPS}}(t)$ is assumed to be

$$\tilde{F}_{\text{ex}}^{\text{EKFPS}}(t) = \rho g \sum_{j=1}^{n_p} a_j \vec{n}_j \sum_{i=1}^{n_{\omega}} \lambda_i e^{\lambda_i Z_j} \cos(\chi_i X_j - \omega_i t + \phi_i) \quad (29)$$

where $\chi_i = \omega_i^2/g$, and X_j and Z_j are the distances of the j th sensor from the x - and z -axes,⁴ respectively. It is also assumed for this $F_{\text{ex}}(t)$ estimator that the pressure at each sensor can be described as

$$P_j(t) = \rho g \sum_{i=1}^{n_{\omega}} \lambda_i e^{\lambda_i Z_j} \cos(\chi_i X_j - \omega_i t + \phi_i) - \rho g(z(t) + X_j) - \frac{C_{R\chi R}(t)}{a_T} \quad (30)$$

where a_T is the total submerged area of the device. Thus, the output vector is given by $\tilde{y} = [\tilde{z} \ \tilde{P}_1 \ \dots \ \tilde{P}_{n_p}]^T$.

The continuous-discrete EKF used by the EKFPS differs from that used for the EKFO strategy. While the outputs of the EKFO [$z(t)$ and $\dot{z}(t)$] are part of the state vector,

⁴Note that the definition of the coordinate system follows the standard convention: the x -axis points in wave direction, and z is the normal to the still water line, with $z = 0$ on the still water line (see Fig. 3)

the output of the EKFPS strategy is given by the nonlinear combination of the states shown in (30). Therefore, the estimation process required by the EKFPS can be summarized as follows.

- 1) Propagate the state \tilde{x}_a (which is as given in (15)) to obtain $\tilde{x}_a^-(k)$ from $\tilde{x}_a(k-1)$ using

$$\dot{\tilde{x}}_a(t) = \begin{bmatrix} \dot{z}(t) \\ \frac{F_T(t)}{m^*} \\ B_R \dot{z}(t) + A_{R\chi R}(t) \\ 0 \end{bmatrix} \quad (31)$$

where $F_T(t)$ is the sum of all the forces, including $F_{\text{PTO}}(t)$, $\tilde{F}_{\text{ex}}^{\text{EKFPS}}(t)$, $F_R(t)$, and $F_H(t)$, which is now given by $F_H(t) = -\rho g \sum_{i=1}^{n_p} a_i \vec{n}_i (z(t) + z_i)$.

- 2) Propagate the covariance matrix to get $\tilde{P}^-(k)$ using the Riccati equation [see (16)], where $\Upsilon(\tilde{x}(t), t)$ needs to be computed, now considering $\tilde{F}_{\text{ex}}^{\text{EKFPS}}$ (instead of $\tilde{F}_{\text{ex}}^{\text{EKFO}}$), and the new description of F_H (instead of the term S_H of the matrix A).
- 3) The Kalman gain is now given by

$$K(k) = P^-(k) \Xi (\tilde{x}_a^-(k))^T \cdot (\Xi (\tilde{x}_a^-(k)) P^-(k) \Xi (\tilde{x}_a^-(k))^T + R)^{-1} \quad (32)$$

where $\Xi = (\partial y / \partial \tilde{x}_a) \in \mathbb{R}^{(n_p+1) \times (n+3n_{\omega})}$ is the Jacobian matrix of the output, evaluated using $\tilde{x}_a^-(k)$.

- 4) Finally, update the covariance $P^-(k)$ and the current state $\tilde{x}_a^-(k)$ using

$$\tilde{x}_a(k) = \tilde{x}_a^-(k) + K(k)(y(k) - \tilde{y}(\tilde{x}_a^-(k))) \quad (33a)$$

$$P(k) = (\mathbf{I}_{n+3n_{\omega}} - K(k)\Xi(\tilde{x}_a^-(k)))P^-(k). \quad (33b)$$

K. Classification of Estimators

From the descriptions of the $F_{\text{ex}}(t)$ estimators given in Sections II-A–II-J, different classifications of the estimators can be proposed. A first class distinguishes between the open-loop and closed-loop estimators. While the CPWE and the PADE are the only open-loop strategies, the remaining estimators are closed-loop. It can be argued that closed-loop estimators have an advantage, since, due to the feedback mechanism, closed-loop estimators can better handle possible uncertainty/noise.

Another possible classification is the use of linear versus nonlinear WEC models. Some estimators require a nonlinear combination of the states to characterize $F_{\text{ex}}(t)$. Thus, the group of linear (model) estimators is composed of the KFRW, KFHO, RHE, UIO, FAUIE, ULISE, and PADE strategies, while the EKFO and EKFPS estimation techniques are inherently nonlinear. The CPWE approach can be linearized by approximating the convolution product using a parametric model, as shown in [17].

A final classification relies on the required measurements. Three different groups of estimators can be distinguished via this classification scheme: using $\eta(t)$ measurements, using device motion measurements, or using both device motion and pressure measurements. The group of estimators using $\eta(t)$ measurements only includes just the CPWE. The group

using only WEC motion measurement embraces the KFRW, KFHO, EKFO, RHE, FAUIE, UIO, and ULISE strategies. Using WEC motion and pressure measurements, the PADE and the EKFPS constitute the last group of this class.

Since the availability of measurement data is defined at the stage of device design and construction, some measurements, required for the $F_{\text{ex}}(t)$ estimator, may not be available and, hence, rule out some strategies. Consequently, the remainder of this article follows the classification based on the required measurements, since this appears to be most important for the practical implementation of the estimator.

III. COMPARISON METHODOLOGY

To compare the performance of the $F_{\text{ex}}(t)$ estimators, the calculation of a reference value for the "true" $F_{\text{ex}}(t)$ value is required to determine the accuracy of each $F_{\text{ex}}(t)$ estimator. However, as mentioned in Section I, the excitation force is, in general, an immeasurable quantity for an oscillating device.

To date, common practice in the literature for the determination of an $F_{\text{ex}}(t)$ reference is to simply generate a random $F_{\text{ex}}(t)$ signal or calculate the signal from $\eta(t)$ data. By using a (linear or nonlinear) hydrodynamic model for motion simulations, the corresponding response of the device is determined using the $F_{\text{ex}}(t)$ reference signal as an input to the simulation model. $F_{\text{ex}}(t)$ is subsequently estimated back from the simulated motion of the device and compared with the $F_{\text{ex}}(t)$ reference.

Although this procedure is a common practice in the field, an important drawback can be identified. Assuming that a specific hydrodynamic model is used for the simulation of the device motion and an identical model is also used in the estimation strategy, an unbiased comparison of these estimators with the ones with different underlying hydrodynamic models is impossible.

To avoid the use of the same model in both the WEC motion simulation and the $F_{\text{ex}}(t)$ estimation stages, a CFD-based numerical wave tank (CNWT) is employed for motion simulation. This not only decouples the reference definition and estimation stages but also delivers more realistic results compared with commonly used hydrodynamic models [34].

For the $F_{\text{ex}}(t)$ reference definition, the following methodology, adopted from [7], [14], and [22], is used in this article.

A set of waves is generated in the CNWT, in which the device is fixed in its equilibrium position. For this diffraction test case, since the device is not moving, radiation and hydrostatic forces are zero and the total wave force $F_w(t)$ measured on the device is $F_{\text{ex}}(t)$. Since $F_w(t)$, and thus $F_{\text{ex}}(t)$, is given by the integral of the pressure over the wetted surface of the device, it can be measured using numerical pressure measurements at specific locations on the hull of the device. For that, a finite number of numerical pressure probes are used to mimic a realistic, physical, test setup. A detailed description of the CNWT and the case study are given in Section IV.

Using the same input wave series, as for the above-described wave diffraction test, simulations are performed with an unconstrained device, free to move.⁵ From these

⁵Note that unconstrained here does not necessarily imply motion in all six degrees of freedom (DoFs), but rather motion in the design DoFs.

TABLE I
STANDARD DEVIATION OF THE MEASUREMENT NOISE

Measurement	η (m)	z (m)	\dot{z} (m/s)	\ddot{z} (m/s ²)	P (Pa)
Standard deviation	0.003	0.003	0.005	0.007	100

simulations, measurements of the required quantities for the different estimators are taken, i.e., $\eta(t)$, WEC motion ($z(t)$, $\dot{z}(t)$, $\ddot{z}(t)$), and pressure. The acquired data are then used in the different $F_{\text{ex}}(t)$ estimators, and the results are compared with the $F_{\text{ex}}(t)$ measured in the wave diffraction tests.

It is important to note that the calculation of $F_{\text{ex}}(t)$ obtained from the wave diffraction test, as a reference for the motion simulation, only holds under linear conditions. For large amplitude relative motion between the body and $\eta(t)$, the excitation force may become nonlinear and equality between $F_{\text{ex}}(t)$ in the wave diffraction and motion tests will not hold. To ensure and verify a linear behavior, some metrics and methodologies are provided in the literature, which are detailed in Section IV.

In order to quantify the accuracy of the analyzed strategies, the estimated $\tilde{F}_{\text{ex}}(t)$ is compared with the $F_{\text{ex}}(t)$ measured with the fixed body, in terms of the normalized root-mean-square accuracy (NRMSA), which is given as

$$\text{NRMSA} = 1 - \sqrt{\frac{\sum_{k=N_S}^{L_S} (F_{\text{ex}}(k) - \tilde{F}_{\text{ex}}(k))^2}{\sum_{k=N_S}^{L_S} F_{\text{ex}}(k)^2}} \quad (34)$$

where L_S is the number of total samples of the simulation and N_S the first sample considered to evaluate the NRMSA. In this work, N_S is set to $0.6L_S$, which is sufficient to avoid the transient time and, therefore, obtain meaningful results. Following (34), the highest accuracy is achieved by an estimator with $\text{NRMSA} = 1$.

Throughout the comparison, $F_{\text{ex}}(t)$ will be estimated using not only the noiseless measures of $\eta(t)$, WEC motion ($z(t)$, $\dot{z}(t)$, $\ddot{z}(t)$), and pressure from the CNWT but also the noisy input data. For that, the numerical measurements will be artificially polluted in a postprocessing step to the motion simulation. This delivers more realistic characteristics of the input data than the real measurement from physical sensors. In particular, the noise added to the measurement signals is normally distributed, with zero mean and standard deviations, as specified in Table I.

IV. CASE STUDY

In this section, the case study for the critical comparison of the $F_{\text{ex}}(t)$ estimators will be described. First, the device under investigation is introduced, followed by a description of the CNWT used for diffraction and motion simulation.

A. WEC Device

A heaving sphere point absorber WEC device (see Fig. 2), with a diameter of 5 m and a draft of 2.5 m, is considered. The hydraulic PTO system is modeled using the nonlinear wave-to-wire model proposed in [35]. Resistive control, with a damping factor of 170 kNs/m, is employed on the PTO system.

The interested reader is referred to [35] for more details on the PTO system. The sea state is chosen to be the representative of real sea conditions. To this end, waves are generated based on a JONSWAP spectrum [36], with a significant wave height of $H_s = 1.5$ m and a peak period of $T_p = 8$ s.⁶ The water depth is set to 70 m. The simulation length is 160 s, with a sampling time of 0.01 s.

B. CNWT

NWTs are commonly used in ocean engineering to analyze wave–structure interaction (WSI) [37]. Lower fidelity NWTs are useful tools for parametric studies, which require fast computations. Commonly solving the Laplace equation in a BEM framework, to account for the WSI, and, therefore, requiring relatively modest computational power, lower fidelity models cannot fully replicate realistic conditions. In contrast, high-fidelity CNWTs are able to provide a realistic, numerical, test bench for WSI experiments, but are associated with relatively high computational cost. However, with the continuing increase in computer power, CNWTs for WEC experiments are nowadays more commonly implemented (see the review in [38]).

The CNWT model in this study is based on the open-source CFD software, OpenFOAM [39]. The hydrodynamics in the CNWT are captured by solving the incompressible Reynolds averaged Navier–Stokes (RANS) equations (35a) and (35b), describing the conservation of mass and momentum, respectively. The volume of fluid (VoF) method, proposed by Hirt and Nichols [40], is used to capture the water wave advection [see (35c) and (35d)]

$$\nabla \cdot \mathbf{u} = 0 \quad (35a)$$

$$\frac{\partial(\rho\mathbf{u})}{\partial t} + \nabla \cdot (\rho\mathbf{u}\mathbf{u}) = -\nabla p + \nabla \cdot \mathbf{T} + \rho\mathbf{f}_b \quad (35b)$$

$$\frac{\partial \alpha}{\partial t} + \nabla \cdot (\mathbf{u}\alpha) = 0 \quad (35c)$$

$$\Phi = \alpha\Phi_{\text{water}} + (1 - \alpha)\Phi_{\text{air}} \quad (35d)$$

where \mathbf{u} is the fluid velocity, p the fluid pressure, ρ the fluid density, \mathbf{T} the stress tensor, and \mathbf{f}_b is the external forces such as gravity. α denotes the volume fraction of water and Φ is a fluid quantity, such as density or viscosity.

Turbulence is modeled using a standard k - ω SST turbulence model with standard wall functions for the turbulent kinetic energy k , the turbulence frequency ω , and the eddy viscosity ν .

A range of numerical wave makers are available to generate and absorb waves in a CNWT [41]. For the present case study, the relaxation zone method, as implemented in the *waves2FOAM* toolbox [42], is employed. The relaxation zone layout is shown in Fig. 2(a).

The symmetry of the test case is exploited by implementing a symmetry boundary condition in the domain, which reduces the computational burden while retaining the accuracy of the results. A schematic of the CNWT domain, with all relevant dimensions, is shown in Fig. 2(b). For more details on the spatial and temporal problem discretization, as well as the mesh layout, the interested reader is referred to [35].

⁶It should be noted that both H_s and T_p are selected so that the obtained simulation is linear, as explained in Section III.

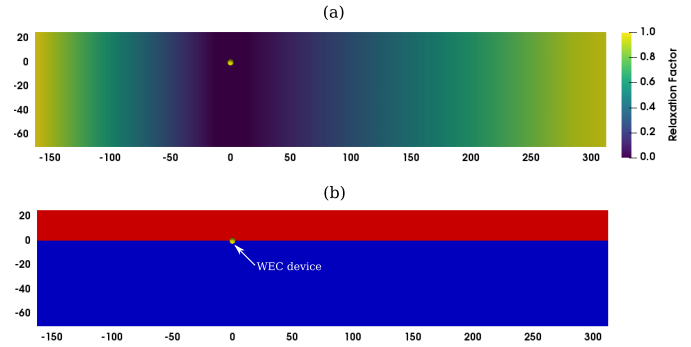


Fig. 2. CNWT domain.

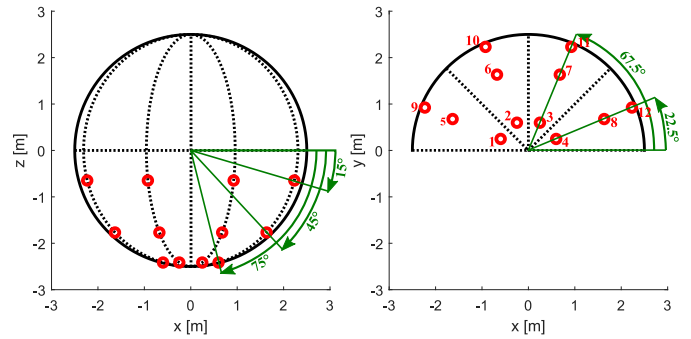


Fig. 3. Locations of the numerical pressure probes. The still water line is located at $z = 0$ m.

To measure $\eta(t)$, the CNWT is equipped with numerical wave probes. Wave Probe 1 (WP1) is located in line with the device center at a distance of 5 m in y -direction, perpendicular to the wave direction. WP2 is located up-wave from the WEC's center at a distance of 20 m. The measurements for the WEC position, velocity, and acceleration are directly given from the motion solver. For the pressure measurements, numerical pressure probes are positioned at specific locations on the WEC hull, as shown in Fig. 3.

Although the CNWT is used for the diffraction and motion simulation, BEM hydrodynamic coefficients, required by the different estimators, have also to be computed. This is done with a BEM-based NWT using the open-source software NEMOH. In addition, the state-space model, to approximate the radiation convolution term, has been calculated using moment-matching, following the method in [10].

C. Linearity of the Case Study

It was stated, in Section III, that linear conditions are required in order to use the $F_{\text{ex}}(t)$ obtained from the wave diffraction tests as a reference for the case of a moving WEC. To verify the linearity of the considered case study, the nonlinearity measure proposed in [43] can be consulted. By comparing the steady-state response of a model against the *best linear approximation*, identified through a minimization problem, the nonlinearity of the wave–device interaction can be quantified. The obtained nonlinearity measure is 0.01 (with a range from 0 to 1) for the case study at hand, confirming that the case is practically linear.

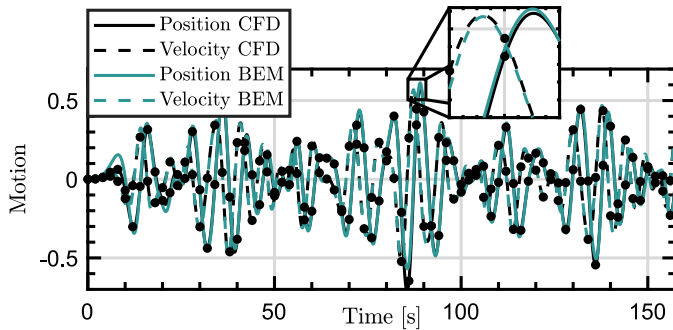


Fig. 4. Comparison between position and velocity obtained from CFD and from the simulation with the linear BEM-based model for polychromatic waves.

To further validate the linearity of the case study, a linear hydrodynamic model, based on (1), was developed using data obtained from a BEM solver. The device is excited with the $F_{ex}(t)$ measured from the CNWT wave diffraction test. The resulting device motion from the linear model can then be compared with the motion measured in the CNWT. If the models coincide, the linearity is further validated.

In Fig. 4, the position and the velocity obtained using both the BEM model and the CFD simulation are plotted. A relatively small deviation in the peaks of the signal can be seen, which are expected due to some nonlinear effects, such as viscous effects, which are neglected in the linear hydrodynamic model.

V. CRITICAL COMPARISON

For the sake of clarity, the results obtained by the different $F_{ex}(t)$ estimators are shown in three different sections, classified by the required measurements (as explained in II-K). Section V-A considers only $F_{ex}(t)$ estimators requiring $\eta(t)$ measurements, while Section V-B considers the estimators using the measurements of the WEC motion only. Section V-C considers the $F_{ex}(t)$ estimators using the measurements of the WEC motion and pressure on the WEC hull. In addition, in Section V-D, a summarizing table along with some discussions are presented.

A. Using $\eta(t)$ Measurements

Although only one estimator uses $\eta(t)$ measurements (CPWE), three different approaches are analyzed here, to show how the forecasting accuracy affects the estimation accuracy:

- 1) $CPWE_{perf}$: Assuming perfect knowledge of $\eta(t)$ at the WEC location [using $\eta(t)$ measured in a simulation with no body].
- 2) $CPWE_{past}$: Considering only past $\eta(t)$ values at the WEC location (measured at WP1).
- 3) $CPWE_{up}$: Using up-wave measurements (measured at WP2).

It should be noted that the $CPWE_{past}$ requires knowledge of $\eta(t)$ values at the WEC location, which, since in the analyzed case waves are unidirectional, can be considered approximately equal to the wave elevation measured at probe WP1. In addition, because of the same assumption of unidirectional

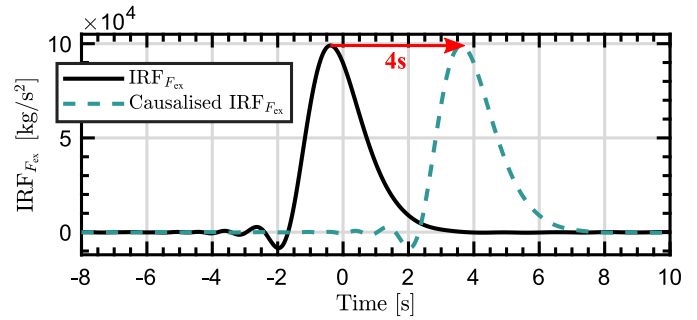


Fig. 5. Non-causal (black solid line) and causalized (blue dashed line) $IRF_{F_{ex}}(t)$ for the analyzed spherical WEC device.

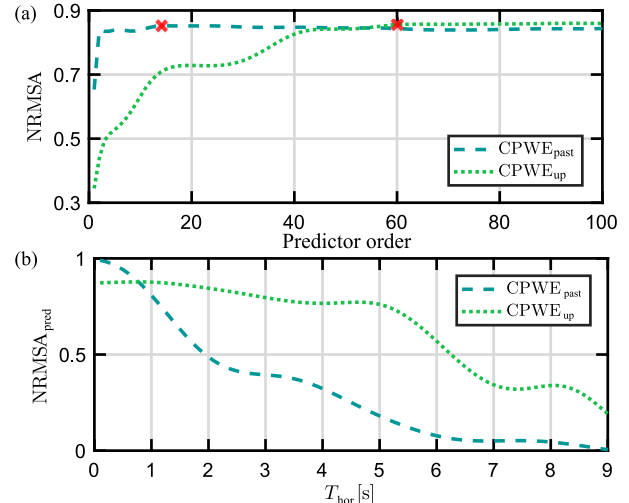


Fig. 6. (a) Estimation accuracy for both $CPWE_{past}$ and $CPWE_{up}$ depending on the order used for the predictor. (b) Prediction accuracy for different T_{hor} obtained using $CPWE_{past}$ and $CPWE_{up}$.

waves, a unique up-wave measurement point can provide full information of the expected $\eta(t)$ at the WEC.

Initially, the required T_{hor} must be determined. When computing the convolution of (5), the value at time 0 of the $IRF_{F_{ex}}(t)$, shown in Fig. 5, is multiplied by the instantaneous $\eta(t)$. The $IRF_{F_{ex}}(t)$ values for positive time instances are multiplied by past $\eta(t)$ values, and the forecasted $\eta(t)$ is multiplied by the $IRF_{F_{ex}}(t)$ values at negative time instances. For this case, shifting the response $T_{hor} = 4s$ is enough to move all the nonzero components of the $IRF_{F_{ex}}(t)$ to positive time instances or, in other words, to causalize it.

The forecasting strategy used in this work is the direct linear multi-step (DLMS) predictor introduced in [18].⁷ Note that, as in [25], $\eta(t)$ is resampled with $T_s = 0.1$ s (from $T_s = 0.01$ s), in order to reduce the size of the predictor.

As shown in Fig. 6(a), the best predictor orders are 15, for the $CPWE_{past}$, and 60, for the $CPWE_{up}$, achieving an NRMSA of 0.857 and 0.872, respectively. One could argue that the results obtained by both the $CPWE_{past}$ and the $CPWE_{up}$ are similar, while, in theory, using up-wave measurements should lead to considerably better results than using only past information. However, $CPWE_{past}$ achieves accurate estimation, because, even though the NRMSA of

⁷For the case of $CPWE_{up}$, it is identified using up-wave η values in a similar fashion to [25]

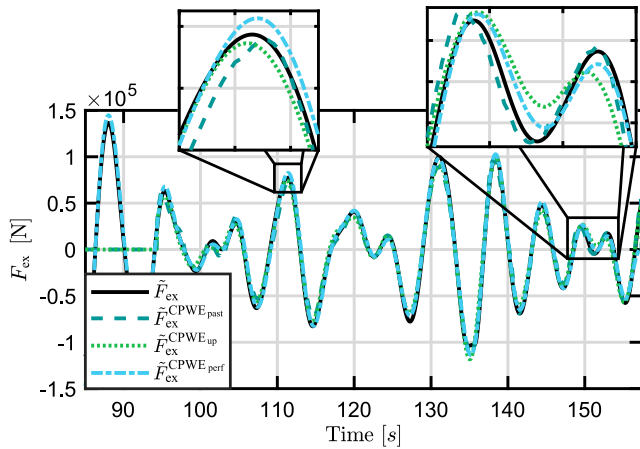


Fig. 7. $F_{ex}(t)$ estimation using $CPWE_{past}$, $CPWE_{up}$, and $CPWE_{perf}$ with an obtained estimation accuracy of 0.857, 0.872, and 0.876, respectively, when no measurement noise is considered.

the prediction ($NRMSA_{pred}$) decreases faster than that of the $CPWE_{up}$, the results obtained over $T_{hor} = [0, 1]$ are better [see Fig. 6(b)], i.e., where the values of $IRF_{F_{ex}}(t)$ are higher and, therefore, where the prediction accuracy has more effect on the NRMSA (see time 0 to -1 s in Fig. 5). In addition, it should be noted that the NRMSA achieved by the $CPWE_{perf}$ is 0.876, which means that the $CPWE_{up}$ obtains similar results compared to $CPWE_{perf}$.

Fig. 7 shows the estimated $F_{ex}(t)$ obtained using the $CPWE_{past}$, the $CPWE_{up}$, and the $CPWE_{perf}$, when no measurement noise is considered. It can be observed that, although the achieved accuracy is similar for the three CPWE variations, the estimated $F_{ex}(t)$ shows some differences.

Surprisingly, even though the CPWE strategies do not have a term to account for the measurement noise, the obtained results, when considering measurement noise, are similar to those obtained when no noise is considered (see Fig. 8). This can be explained by the fact that the DLMS prediction strategy acts as a low pass filter if the order is correctly chosen.

Since, for most of the following estimators, the results obtained considering noise are similar to those obtained without noise and the cases considering noise reflect a more realistic scenario, for the sake of brevity, only results considering noise will be shown in the following.

B. Using Motion Measurements

For the sake of clarity, the results of this section are divided into two different sets: those estimators using a model to describe the dynamics of $F_{ex}(t)$ (KFRW, KFHO, and EKFHO), and the strategies that do not assume any dynamical model for $F_{ex}(t)$ (RHE, FAUIE, UIO, and ULISE).

1) *Considering a Model for $F_{ex}(t)$* : First, an analysis of the effect of the HO order, n_{ω} , on estimation accuracy is carried out, when using the KFHO and EKFHO strategies. As shown in Fig. 9, while the NRMSA achieved by the KFHO improves when increasing n_{ω} , no corresponding improvement can be observed for the EKFHO. This is consistent with the findings in [26]. Compared with the EKFHO, where the frequencies ω are adaptive, the KFHO strategy has an additional potential

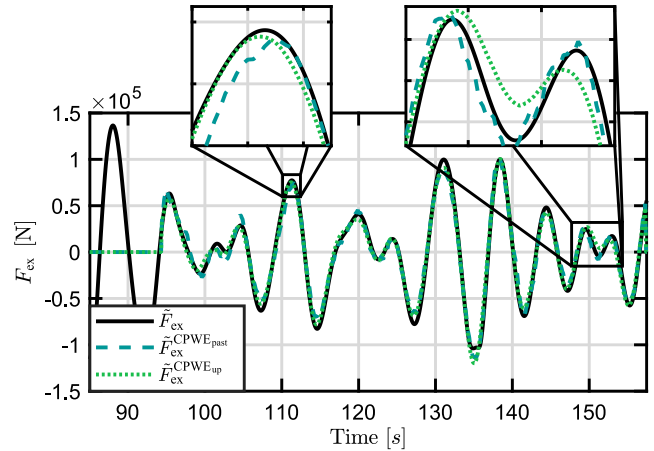


Fig. 8. $F_{ex}(t)$ estimation using both $CPWE_{past}$ and $CPWE_{up}$, with an obtained estimation accuracy of 0.854 and 0.871, respectively, considering measurement noise.

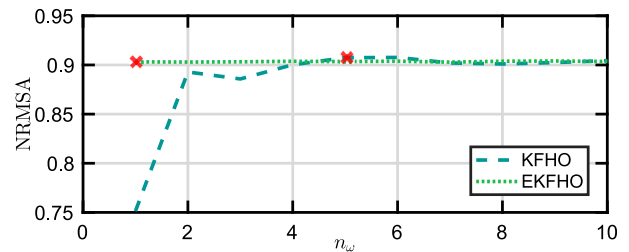


Fig. 9. Obtained NRMSA by the KFHO and EKFHO strategies for different HO orders n_{ω} . The chosen orders for KFHO and EKFHO are $n_{\omega} = 5$ and 1, respectively (red cross).

pitfall, which is the choice of the frequencies of the HO. For the presented test case, these frequencies are chosen to be linearly spaced between 0.5 and 2 rad. However, the NRMSA shown in Fig. 9 may increase if the value of the frequencies used by KFHO is optimized for every n_{ω} [25].

Although the KFRW, KFHO, and EKFHO estimators obtain similar NRMSAs for the case without noise (0.891, 0.907, and 0.903, respectively), this is not the case when measurement noise is introduced. As shown in Fig. 10, the EKFHO shows the lowest accuracy among the three, being the most affected by measurement noise (the NRMSA is 0.066 less when considering noise). Although the NRMSA achieved by the KFRW is only reduced by 0.026, when introducing noise, the resulting estimated $F_{ex}(t)$ is the noisiest among the three signals (see Fig. 10). In contrast, since the model of the KFHO gives the filter some information about the expected $F_{ex}(t)$ dynamics, the KFHO estimate is the least noisy, resulting in a decrease of 0.006 in accuracy with respect to the result obtained when no noise is considered.

2) *Without Considering a Model for $F_{ex}(t)$* : As shown in Fig. 11, the FAUIE strategy produces a relatively noisy estimate, and the NRMSA decreases by 0.125 compared with the noise-free case (see Fig. 12). This is expected since there is no explicit term to account for the measurement noise, as shown in Section II-F. The results obtained by FAUIE could possibly be improved by low-pass filtering the measurements in a preprocessing step; however, it would increase considerably the delay of the excitation force estimate.

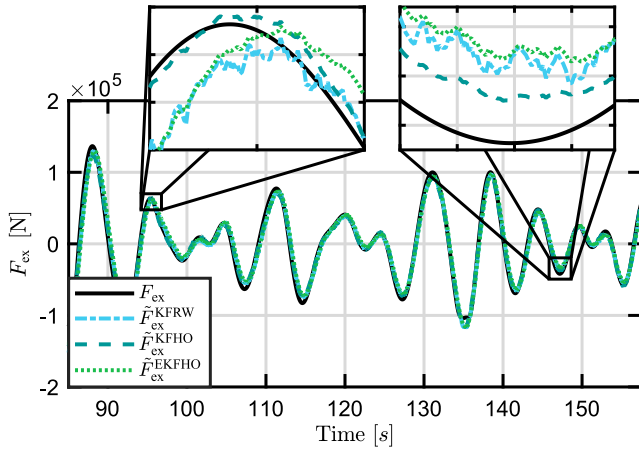


Fig. 10. $F_{ex}(t)$ estimation using the KFRW, KFHO, and EKFHO strategies obtaining an NRMSA of 0.865, 0.902, and 0.837, respectively, considering measurement noise.

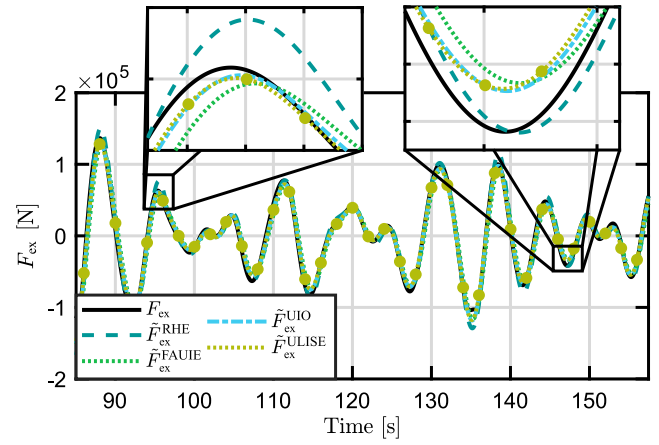


Fig. 12. $F_{ex}(t)$ estimation using the RHE, FAUIE, UIO, and ULISE strategies obtaining an NRMSA of 0.847, 0.813, 0.896, and 0.903, respectively, where no measurement noise is considered.

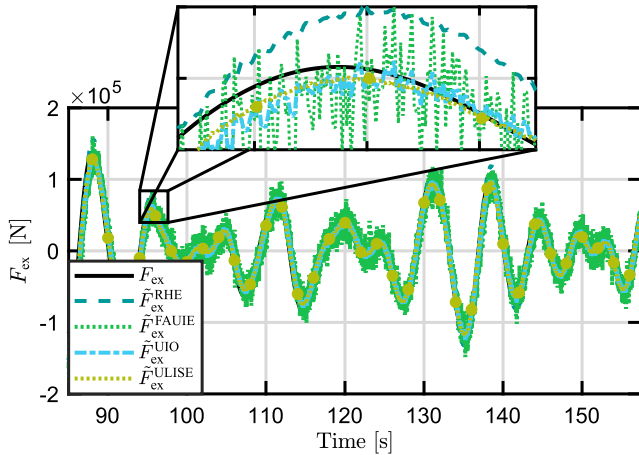


Fig. 11. $F_{ex}(t)$ estimation using the RHE, FAUIE, UIO, and ULISE strategies obtaining an NRMSA of 0.828, 0.688, 0.856, and 0.901, respectively, considering measurement noise.

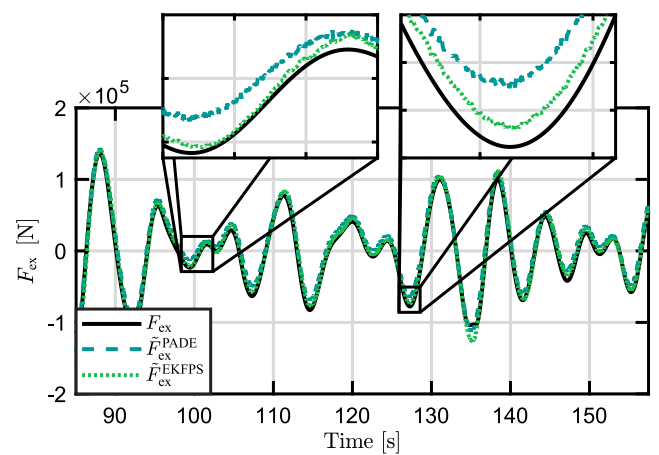


Fig. 13. $F_{ex}(t)$ estimation using the PADE and EKFPS strategies obtaining an NRMSA of 0.792 and 0.822, respectively, considering measurement noise.

Even though the UIO approach includes a term to account for the measurement noise, from the visual inspection of Figs. 11 and 12, it can be seen that the UIO estimate is considerably affected by the presence of measurement noise and, thus, the NRMSA decreases by 0.04.

For the RHE strategy, the window length is selected, such that, for the chosen design parameters and for the case where no noise is considered, the obtained NRMSA is maximized and, for this case, $N = 8$ obtaining NRMSA = 0.859.

The NRMSA achieved by the RHE strategy is relatively unaffected by the introduction of measurement noise and only decreases from 0.847 to 0.828. Similarly, the effectiveness of the ULISE in coping with measurement noise should be highlighted, with a loss of just 0.002 in NRMSA when measurement noise is considered.

C. Using Motion and Pressure Measurements

Regarding the set of estimators using motion and pressure measurements, it has been found that, for the PADE strategy, the number of pressure sensors directly affects the total wave force $F_w(t)$ estimate. In the presented test case, the error in the estimation of $F_w(t)$ leads to an offset of the $\tilde{F}_{ex}^{PADE}(t)$ compared with $F_{ex}(t)$ (see Fig. 13). However, even though

the noisy measurements are directly used to estimate $F_{ex}(t)$, the obtained results are not affected, which may be explained by possible destructive interference of the different noisy signals.

On the other hand, the EKFPS strategy (of order $n_\omega = 4$) gives a more accurate estimate, obtaining an NRMSA of 0.872 (compared with the 0.793 obtained by PADE), for the case where measurement noise is not considered, and 0.822, for the case where noise is included.

D. Summary

This section summarizes the results in the tabulated form. For each $F_{ex}(t)$ estimator, Table II shows the measurements required and the obtained accuracy for the cases with and without measurement noise. Furthermore, the time delay of $\tilde{F}_{ex}(t)$ relative to the reference is given, obtained via cross-correlation. From an EMCS perspective, the delay time is an important information, since a delay in the $\tilde{F}_{ex}(t)$ signal could affect the performance of the controller [7]. Finally, the required time for estimation, normalized against the fastest strategy, is listed.

In terms of delay time, one can note that the open-loop estimators (CPWE and PADE) are the only strategies obtaining a negative delay, while the KFHO, EKFHO, and ULISE are

TABLE II
COMPARISON TABLE WITH THE RESULTS OBTAINED
BY THE DIFFERENT ESTIMATORS

Name	Input Data					Accuracy		Delay [s]	Time _r
	$\eta(t)$	z	\dot{z}	\ddot{z}	P	NRMSA	NRMSA _n		
CPWE _{past}	•	-	-	-	-	0.857	0.854	-0.03	1
CPWE _{up}	•	-	-	-	-	0.872	0.871	-0.06	1
KFRW	-	•	•	-	-	0.891	0.865	0.04	25
KFHO	-	•	•	-	-	0.907	0.902	0	28
EKFHO	-	•	•	-	-	0.903	0.837	0	4·10 ³
RHE	-	•	•	-	-	0.847	0.828	0.07	30
FAUIE	-	•	•	•	-	0.813	0.688	0.16	1·10 ³
UIO	-	•	•	-	-	0.896	0.856	0.09	117
ULISE	-	•	-	•	-	0.903	0.901	0	98
PADE	-	•	•	•	•	0.793	0.792	-0.01	29
EKFPS	-	•	-	-	•	0.872	0.822	0.03	9·10 ³

in phase with respect to $F_{ex}(t)$ and the KFRW, RHE, FAUIE, UIO, and EKFPS are delayed.

Regarding the estimation time, it is found that the CPWE is the fastest strategy to estimate the $F_{ex}(t)$ signal (requiring about $1 \cdot 10^{-6}$ s for one $F_{ex}(t)$ estimation step⁸), followed by the KFRW, KFHO, PADE, RHE, ULISE, and UIO, which, although they are slower than the CPWE, may still be considered fast, in absolute terms. Finally, the FAUIE, EKFHO, and EKFPS are the slowest strategies, which, in the case of EKFHO and EKFPS is expected, since the estimators are inherently nonlinear and require linearization of the function describing $F_{ex}(t)$ at each step. In the FAUIE, the computational burden is associated with the derivative error \dot{e}_y [see (21)], which creates an algebraic loop, slowing down the estimation process.

In terms of measurement requirements, WEC motion measurements are the easiest/cheapest to obtain, using inertial measurement units (IMUs). In contrast, it should be noted that pressure sensors are relatively expensive and the estimators using pressure measurements do not show any particular improvement with respect to the strategies using motion measurements alone. In addition, past $\eta(t)$ values, at the WEC location, are physically immeasurable, and, therefore, in a real sea scenario, the estimate has to be calculated on either up-wave measurements or WEC motion. To estimate/predict $\eta(t)$, based on up-wave measurements in a real-sea scenario, several measurement points are required [19], which are expensive to obtain. In addition, using motion measurements to estimate $\eta(t)$ is suboptimal since two estimation stage errors are accumulated, while directly estimating $F_{ex}(t)$ based on WEC motion is a more straightforward approach.

VI. CONCLUSION

This article presents a critical and fair comparison of all $F_{ex}(t)$ estimators found in the literature. Because of theoretical restrictions, only a linear case is shown. To remove any bias from the comparison, the $F_{ex}(t)$ reference signal has been obtained using a CNWT, and thus decouples the model used to evaluate the estimator performance and the model internally used by the $F_{ex}(t)$ estimator.

⁸The test have been carried out in a computer with an Intel CORE i7 and 8-GB RAM.

Based on the obtained results, it can be concluded that estimation techniques based on the WEC motion are the most feasible, specifically the KFHO, ULISE, and UIO. The KFHO and the ULISE show good performance in terms of achieved accuracy and small delay times, i.e., no phase shift between the estimated and the reference signal. Even though the UIO is not the most accurate estimator, it is the only approachable to consider model uncertainty, which could be important in a real WEC device scenario. From Section V, one can note that other estimation strategies also obtain accurate results. However, since they do not show any improvement with respect to the KFHO, ULISE, or UIO approaches, they are not highlighted in this section.

A further study is required to assess how the different strategies behave under nonlinear conditions, for which the present CNWT framework is well suited. However, obtaining the reference $F_{ex}(t)$ poses a challenge and perhaps loses meaning in a case where the linear superposition and decomposition of hydrodynamic force no longer apply. While the FAUIE already includes a term to account for non-linearities, KF-based strategies can easily be extended to include nonlinear WEC models in a fashion similar to the EKFHO and EKFPS. The extension of the remaining approaches should be further analyzed. Finally, it is of interest if, under nonlinear conditions, knowledge of pressure on the WEC hull improves the $F_{ex}(t)$ estimate compared with the strategies using only motion measurements. In addition, it is of interest to know how the estimators perform, when considering multi-DoF.

REFERENCES

- [1] A. Clement *et al.*, "Wave energy in Europe : Current status and perspectives," *Renew. Sustain. Energy Rev.*, vol. 6, no. 5, pp. 405–431, Oct. 2002.
- [2] G. J. Dalton, R. Alcorn, and T. Lewis, "Case study feasibility analysis of the Pelamis wave energy converter in Ireland, Portugal and North America," *Renew. Energy*, vol. 35, no. 2, pp. 443–455, Feb. 2009.
- [3] A. Raventos, A. Sarmento, F. Neumann, and N. Matos, "Projected deployment and costs of wave energy in Europe," in *Proc. 3rd Int. Conf. Ocean Energy*, Oct. 2010, pp. 1–6.
- [4] J. V. Ringwood, G. Bacelli, and F. Fusco, "Energy-maximizing control of wave-energy converters: The development of control system technology to optimize their operation," *IEEE Control Syst.*, vol. 34, no. 5, pp. 30–55, Oct. 2014.
- [5] N. Faedo, S. Olaya, and J. V. Ringwood, "Optimal control, MPC and MPC-like algorithms for wave energy systems: An overview," *IFAC J. Syst. Control*, vol. 1, pp. 37–56, Sep. 2017.
- [6] M. Garcia-Abril, M. Paparella, and F. Ringwood, "Excitation force estimation and forecasting for wave energy applications," *IFAC-PapersOnLine*, vol. 50, no. 1, pp. 14692–14697, Jul. 2017.
- [7] H.-N. Nguyen and P. Tona, "Wave excitation force estimation for wave energy converters of the point-absorber type," *IEEE Trans. Control Syst. Technol.*, vol. 26, no. 6, pp. 2173–2181, Nov. 2017.
- [8] B. Guo, R. J. Patton, S. Jin, and J. Lan, "Numerical and experimental studies of excitation force approximation for wave energy conversion," *Renew. Energy*, vol. 125, pp. 877–889, Sep. 2018.
- [9] W. Cummins, "The impulse response function and ship motions," DTIC, Fort Belvoir, VA, USA, Tech. Rep. 1661, 1962.
- [10] N. Faedo, Y. Peña-Sanchez, and J. V. Ringwood, "Finite-order hydrodynamic model determination for wave energy applications using moment-matching," *Ocean Eng.*, vol. 163, pp. 251–263, Sep. 2018.
- [11] C.-T. Chen, *Linear System Theory and Design*. Oxford, U.K.: Oxford Univ. Press, 1998.
- [12] A. Babarit and G. Delhommeau, "Theoretical and numerical aspects of the open source BEM solver NEMOH," in *Proc. 11th Eur. Wave Tidal Energy Conf.*, 2015, pp. 1–36.
- [13] C.-H. Lee and J. N. Newman, "Wamit user manual," WAMIT, Inc, Chestnut Hill, MA, USA, Tech. Rep., 2006.

- [14] S. Giorgi, J. Davidson, and J. V. Ringwood, "Identification of nonlinear excitation force kernels using numerical wave tank experiments," in *Proc. 11th Eur. Wave Tidal Energy Conf. (EWTEC)*, 2015, pp. 1–10.
- [15] M. Abdelrahman, R. Patton, B. Guo, and J. Lan, "Estimation of wave excitation force for wave energy converters," in *Proc. 3rd Conf. Control Fault-Tolerant Syst. (SysTol)*, Sep. 2016, pp. 654–659.
- [16] J. Falnes, "On non-causal impulse response functions related to propagating water waves," *Appl. Ocean Res.*, vol. 17, no. 6, pp. 379–389, Dec. 1995.
- [17] B. Guo, R. Patton, and S. Jin, "Identification and validation of excitation force for a heaving point absorber wave energy converter," in *Proc. 12th Eur. Wave Tidal Energy Conf. EWT*, 2017, pp. 1–9.
- [18] Y. Peña-Sánchez, A. Mérigaud, and J. V. Ringwood, "Short-term forecasting of sea surface elevation for wave energy applications: The autoregressive model revisited," *IEEE J. Ocean. Eng.*, to be published.
- [19] A. Mérigaud and J. V. Ringwood, "Incorporating ocean wave spectrum information in short-term free-surface elevation forecasting," *IEEE J. Ocean. Eng.*, vol. 44, no. 2, pp. 401–414, Apr. 2018.
- [20] D. Cavaglieri, T. R. Bewley, and M. Previsic, "Model predictive control leveraging ensemble Kalman forecasting for optimal power take-off in wave energy conversion systems," in *Proc. Amer. Control Conf. (ACC)*, Jul. 2015, pp. 5224–5230.
- [21] J. L. Crassidis and J. L. Junkins, *Optimal Estimation of Dynamic Systems*. Boca Raton, FL, USA: CRC Press, 2004.
- [22] P. Kracht, S. Perez-Becker, J.-B. Richard, and B. Fischer, "Performance improvement of a point absorber wave energy converter by application of an observer-based control: Results from wave tank testing," *IEEE Trans. Ind. Appl.*, vol. 51, no. 4, pp. 3426–3434, Jul./Aug. 2015.
- [23] B. A. Ling and B. A. Batten, "Real time estimation and prediction of wave excitation forces on a heaving body," in *Proc. ASME 34th Int. Conf. Ocean, Offshore Arctic Eng.*, May 2015, pp. 1–10.
- [24] B. A. Ling, "Real-time estimation and prediction of wave excitation forces for wave energy control applications," M.S. thesis, Dept. Mech. Eng., Oregon State Univ., Corvallis, OR, USA, 2015.
- [25] Y. Peña-Sánchez, M. Garcia-Abril, F. Paparella, and J. V. Ringwood, "Estimation and forecasting of excitation force for arrays of wave energy devices," *IEEE Trans. Sustain. Energy*, vol. 9, no. 4, pp. 1672–1680, Oct. 2018.
- [26] F. Fusco and J. V. Ringwood, "A simple and effective real-time controller for wave energy converters," *IEEE Trans. Sustain. Energy*, vol. 4, no. 1, pp. 21–30, Jan. 2013.
- [27] S. Mhatre, "Application of a linear optimal estimator on a wave energy converter using bang-singular-bang control," M.S. thesis, Dept. Mech. Eng., Michigan Technol. Univ., Houghton, MI, USA, 2017.
- [28] O. Abdelkhalik, S. Zou, R. Robinett, G. Bacelli, and D. Wilson, "Estimation of excitation forces for wave energy converters control using pressure measurements," *Int. J. Control*, vol. 90, no. 8, pp. 1793–1805, 2016.
- [29] M. Abdelrahman and R. Patton, "Robust control of a wave energy converter with soft sensing of wave excitation force," in *Proc. 12th Eur. Wave Tidal Energy Conf.*, 2017, pp. 974–1–974–10.
- [30] R. Coe and G. Bacelli, "State estimation for advanced control of wave energy converters," Mar. Hydrokinetic Data Repository, Sandia Nat. Lab., Livermore, CA, USA, Tech. Rep. SAND2017-4401, 2017.
- [31] S. Z. Yong, M. Zhu, and E. Frazzoli, "A unified filter for simultaneous input and state estimation of linear discrete-time stochastic systems," *Automatica*, vol. 63, pp. 321–329, Jan. 2016.
- [32] G. Bacelli, R. G. Coe, D. Patterson, and D. Wilson, "System identification of a heaving point absorber: Design of experiment and device modeling," *Energies*, vol. 10, no. 4, p. 472, Mar. 2017.
- [33] O. Abdelkhalik, S. Zou, G. Bacelli, R. D. Robinett, D. G. Wilson, and R. G. Coe, "Estimation of excitation force on wave energy converters using pressure measurements for feedback control," in *Proc. OCEANS MTS/IEEE Monterey*, Sep. 2016, pp. 1–6.
- [34] C. Windt, N. Faedo, M. Penalba, and J. V. Ringwood, "Evaluation of energy maximising control systems for the Wavestar wave energy converter," in *Proc. Amer. Control Conf., Philadelphia*, 2019, pp. 1–14.
- [35] M. Penalba, J. Davidson, C. Windt, and J. V. Ringwood, "A high-fidelity wave-to-wire simulation platform for wave energy converters: Coupled numerical wave tank and power take-off models," *Appl. Energy*, vol. 226, pp. 655–669, Sep. 2019.
- [36] D. E. Hasselmann, M. Dunkel, and J. Ewing, "Directional wave spectra observed during JONSWAP 1973," *J. Phys. Oceanogr.*, vol. 10, no. 8, pp. 1264–1280, 1980.
- [37] K. Tanizawa, "The state of the art on numerical wave tank," in *Proc. 4th Osaka Colloq. Seakeeping Perform. Ships*, 2000, pp. 95–114.
- [38] C. Windt, J. Davidson, and J. Ringwood, "High-fidelity numerical modelling of ocean wave energy systems: A review of computational fluid dynamics-based numerical wave tanks," *Renew. Sustain. Energy Rev.*, vol. 93, pp. 610–630, Oct. 2018.
- [39] H. G. Weller, G. Tabor, H. Jasak, and C. Fureby, "A tensorial approach to computational continuum mechanics using object-oriented techniques," *Comput. Phys.*, vol. 12, no. 6, pp. 620–631, 1998.
- [40] C. W. Hirt and B. D. Nichols, "Volume of fluid (VOF) method for the dynamics of free boundaries," *J. Comput. Phys.*, vol. 39, no. 1, pp. 201–225, Jan. 1981.
- [41] C. Windt, J. Davidson, P. Schmitt, and J. V. Ringwood, "On the assessment of numerical wave makers in CFD simulations," *J. Mar. Sci. Eng.*, vol. 7, no. 2, p. 47, Feb. 2019.
- [42] N. Jacobsen, D. R. Fuhrmann, and J. Fredsø, "A wave generation toolbox for the open-source CFD library: OpenFoam," *Int. J. Numer. Methods Fluids*, vol. 70, no. 9, pp. 1073–1088, Nov. 2012.
- [43] M. Penalba and J. Ringwood, "Linearisation-based nonlinearity measures for wave-to-wire models in wave energy," *Ocean Eng.*, vol. 171, pp. 496–504, Jan. 2019.



Yeraí Peña-Sánchez received the Diploma degree in renewable energies engineering from the University of the Basque Country (EHU), Eibar, Spain, in 2016. He is currently pursuing the Ph.D. degree with the Centre for Ocean Energy Research (COER), Maynooth University, Maynooth, Ireland.

He is involved in the estimation and forecasting of wave excitation forces.



Christian Windt received the B.Sc. degree in mechanical engineering and the M.Sc. degree in energy systems from the Hamburg University of Technology, Hamburg, Germany, in 2013 and 2015, respectively. He is currently working on his Ph.D. thesis at the Center for Ocean Energy Research, Maynooth University, Maynooth, Ireland, on high-fidelity numerical hydrodynamic modeling of wave energy systems.

He gained experience in the field of ocean wave energy conversion as a Visiting Research Student at Queen's University Belfast, Belfast, U.K., and the University of California at Berkeley, Berkeley, CA, USA.



Josh Davidson was born in Townsville, QLD, Australia. He received the degree (Hons.) in physics and the Ph.D. degree in physics from the School of Engineering and Physical Sciences, James Cook University, Townsville.

He was the Deputy Director of the Centre for Ocean Energy Research (COER), Maynooth University, Maynooth, Ireland, where he was involved in the nonlinear hydrodynamic modeling and control of wave energy converters and the development of numerical wave tanks. He is currently a Research

Fellow with the Department of Fluid Mechanics, Budapest University of Technology and Economics, Budapest, Hungary.



John V. Ringwood (S'87–SM'97) received the Diploma degree in electrical engineering from the Dublin Institute of Technology, Dublin, Ireland, and the Ph.D. degree in control systems from University of Strathclyde, Glasgow, U.K., in 1981 and 1985, respectively.

He is currently a Professor of electronic engineering with Maynooth University, Maynooth, Ireland, where he is also the Director of the Centre for Ocean Energy Research. His current research interests include time series modeling, wave energy,

control of plasma processes, and biomedical engineering.

Dr. Ringwood is also a Chartered Engineer and a fellow of Engineers Ireland.